Solution Synthesis and Diffusion-Mediated Formation Pathway of $NbTe_4$ Particles

Katherine L. Thompson,[1] Peyton L. Herring,[1] Mauricio Terrones,[1,2,3,4,*] and Raymond E. Schaak[1,5,6,*]

[1] *Department of Chemistry*, [2] *Department of Physics,* [3] *Department of Materials Science and Engineering,* [4] *Center for 2-Dimensional and Layered Materials*, [5] *Department of Chemical Engineering, and* [6] *Materials Research Institute, The Pennsylvania State University, University Park, PA 16802, United States*

E-mail: res20@psu.edu and mut11@psu.edu

ABSTRACT

$NbTe_4$ is an important material because of its fundamental low-temperature electronic behavior and its potential interest for thermoelectric, catalytic, and phase-change applications, especially as nano- and micro-scale particles. As a tellurium-rich group V transition metal telluride, bulk $NbTe_4$ is typically synthesized through high-temperature solid-state or metal flux reactions and $NbTe_4$ films can be made by sputtering and annealing, but $NbTe_4$ is generally not amenable to the lower-temperature solution-based syntheses that yield small particles. Here, we demonstrate a solvothermal route to $NbTe_4$ particles that is based on mainstream colloidal nanoparticle synthesis. We find that the reaction proceeds *in situ* through a multi-step pathway that begins by first forming elemental tellurium needles. $NbTe_4$ then deposits on the surface of the tellurium needles through a diffusion-based process. Time-point studies throughout the reaction reveal that crystallographic relationships between Te and $NbTe_4$ define how the diffusion-based reaction proceeds and help to rationalize the morphology of the resulting $NbTe_4$ particles. As synthesized, $NbTe_4$ particles exhibit a surface consisting of predominantly Nb-Te and reduced NbO_x species, but after storage, surface oxidation transforms these species to primarily Nb_2O_5 and TeO_2, while the $NbTe_4$ remains unchanged. These synthetic capabilities and reaction pathway insights for $NbTe_4$, made using a solvothermal method, will help to advance future studies on the properties and applications of this and related tellurides.

INTRODUCTION

Nanoscale metal telluride materials are important across many applications, including the fabrication of thermoelectric systems,[1-3] superconductors,[4,5] electrocatalysts,[6,7] and components in electronic devices.[8,9] Quasi-one-dimensional transition metal tellurides are especially attractive materials. A quasi-one-dimensional compound contains repeating chain motifs that are held together by covalent or ionic bonds, rather than by weaker van der Waals interactions like conventional one-dimensional materials.[10] Niobium tetratelluride, $NbTe_4$, is a quasi-one-dimensional material that is being explored due to its unique electrical properties.[11] At normal pressure $NbTe_4$ exhibits multiple charge density wave transitions but transforms to a superconductor under pressure.[12] Arrays of microscale and nanoscale rods of $NbTe_4$ have been shown to exhibit electronic field emission characteristics.[13] Sputtered films of $NbTe_4$ function as a phase change material; application of a voltage can cycle the $NbTe_4$ films between amorphous and crystallite states, which differ in their resistivities by several orders of magnitude.[14]

These properties and applications motivate us to consider how $NbTe_4$ can be synthesized in nanocrystalline form. Bulk metal tellurides such as $NbTe_4$ are synthesized using traditional high temperature solid-state reactions between elemental niobium and tellurium,[15] as well as through crystallization from a high-temperature tellurium flux.[12] Microscale and nanoscale $NbTe_4$ can be grown on Nb substrates using chemical vapor transport at temperatures above 500 ^oC.[13] To date, the solution-based methods that are most common for synthesizing colloidal nanoparticles of many inorganic compounds, including metal chalcogenides, are absent for $NbTe_4$. As mentioned for the phase change films in the preceding paragraph, amorphous $NbTe_4$ can be formed by sputtering and then crystallized at 272 ^oC.[14] This result is intriguing, because it suggests that if Nb and Te can be made to combine in solution, $NbTe_4$ could potentially crystallize, since this crystallization temperature is below the boiling points of most solvents used for solvothermal nanocrystal synthesis. The ability to synthesize $NbTe_4$ (and related) particles colloidally could advance the applications of these materials by enabling liquid-phase processing of films, coatings, and patterned surfaces. Additionally, it could offer solution-mediated control over size, morphology, and faceting that would be useful for understanding how these particle features influence properties at both ensemble and single-particle levels.

Solution routes to niobium telluride nanostructures do not exist, to the best of our knowledge. There are reports of colloidally synthesized niobium sulfides and selenides, but these typically produce the transition metal dichalcogenides NbS_2 and $NbSe_2$ and tend to require highly reactive chalcogen reagents.[16] Metal tellurides, in general, tend to be more challenging to synthesize than their corresponding sulfides and selenides due to both the lower reactivity of tellurium reagents and the propensity toward oxidation of telluride products once formed.[17,18] Indeed, the reactivity of the tellurium reagent can directly impact the amount of tellurium in the product, and therefore the phase that forms;[19] more reactive tellurium reagents (that also tend to be extremely hazardous) are generally required form more tellurium-rich tellurides.[17]

Here, we describe the solution-based synthesis of $NbTe_4$ in oleylamine using $NbCl_5$ and diphenyl ditelluride, which are relatively mild and readily available reagents. To form the tellurium-rich product, the need for an extremely reactive tellurium reagent is sidestepped using a pathway that initially forms tellurium needles, followed by *in situ* reaction with niobium in a subsequent step. This approach, which is facilitated by crystal structure relationships between Te and $NbTe_4$, pre-defines the tellurium-rich stoichiometry of the product through the characteristics of the tellurium needle intermediate and the niobium that is diffusing into it, rather than by the reactivity of the

tellurium reagent. In addition to mapping out the reaction pathway, we probe the surface and bulk stability of the solution synthesized $NbTe_4$ to elucidate the propensity toward oxide formation.

EXPERIMENTAL SECTION

Materials. Niobium (V) chloride, tantalum (V) chloride, diphenyl ditelluride, oleylamine (70% technical grade), 1-octadecene (90% technical grade), and oleic acid (90% technical grade) were purchased from Sigma-Aldrich. Analytical grade toluene and ethanol were purchased from VWR. All chemicals were used as received without further purification.

Synthesis of $NbTe_4$. Initially, 5 mL of oleylamine was loaded into a 25 mL three-neck flask and degassed at 120 °C for 30 minutes. The $NbCl_5$ and diphenyl ditelluride were stored in a glovebox for ease of use and to prevent degradation. For reactions targeting two-fold excess Nb concentrations, 67.5 mg of $NbCl_5$ and 102.4 mg of diphenyl ditelluride were dissolved in 2.5 mL of oleylamine in a vial to obtain 0.5 mmol of both precursors. To achieve a stoichiometric loading targeting $NbTe_4$, the $NbCl_5$ content was reduced to 33.8 mg. The vial was degassed at 100 °C for 1 hour. Both the flask and the vial were cycled between vacuum and Ar three times prior to injection. The flask was then heated to 340 °C at a ramp rate of 23 °C/minute. At 340 °C, the vial contents were rapidly injected into the flask and held at 340 °C for 1 hour. Then the solution was gradually cooled by removing the flask from the heating mantle. The resulting particles were then transferred to a centrifuge tube with 20 mL of a 1:1 ethanol:toluene solution and centrifuged at 14500 rpm for 3 minutes. The washing step was repeated twice, and the particles were stored in ethanol. Additionally, time point studies were carried out to monitor the progress of the reaction. These reactions followed the same conditions as reported above, except the $NbCl_5$ content was 50.7 mg to target a 1.5-fold excess of Nb to obtain a phase pure product with minimal excess Nb. The time points probed were 15, 30, 45, and 60 minutes. To probe the effect of solvent, either oleic acid or 1-octadecene (heated to 300 °C) was loaded to the flask initially, and otherwise utilized the above reaction conditions.

Characterization. An Empyrean diffractometer using Cu Kα radiation was used to collect powder X-ray diffraction (XRD) data for all materials. CrystalMaker and CrystalDiffract from CrystalMaker Software Ltd., Oxford, England, were used to generate the crystal structure graphics and simulate the powder diffraction patterns. Scanning electron microscopy (SEM) images and energy dispersive X-ray spectroscopy (EDS) maps were obtained with an Apreo 5 SEM at an accelerating voltage of 15 keV. Oxford Instruments AZtec software was used to generate SEM-EDS maps and analyze EDS spectra using the Nb Lα, Te Lα, and O Kα lines. All high-angle annular dark-field scanning transmission electron microscopy (HAADF-STEM) images and STEM-EDS elemental maps were collected on an FEI Talos F200XS/TEM at an accelerating voltage of 200 kV. Thermo Scientific Velox software was used to analyze and generate STEM-EDS elemental map data, where the Nb Lα, Te Lα, and O Kα lines were mapped. Samples for X-ray photoelectron spectroscopy (XPS) were prepared by allowing the suspended material to dry in a small, plastic tube and grinding it into a powder. XPS spectra were recorded using a Physical Electronics Versa Probe II instrument equipped with a monochromatic Al Kα X-ray source (hv = 1,486.7 eV) and a concentric hemispherical analyzer. Charge neutralization was performed using both low energy electrons (<5 eV) and argon ions. The binding energy axis was calibrated using sputter cleaned Cu (Cu $2p_{3/2}$= 932.62 eV, Cu $3p_{3/2}$ = 75.1 eV) and Au (Au $4f_{7/2}$ = 83.96 eV) foils. Peaks were charge referenced to the Nb $3d_{5/2}$ peak for Nb_2O_5 at 207.4 eV. The $NbTe_x$ component peaks were fit with

an asymmetric line shape. To affirm that the asymmetric line shape provides an adequate fit for a niobium chalcogenide, we fit an asymmetric line shape to an exfoliated niobium sulfide sample and applied the same line shape to the $NbTe_4$ sample. Measurements were made at a takeoff angle of 45° with respect to the sample surface plane. This resulted in a typical sampling depth of 3-6 nm (95% of the signal originated from this depth or shallower). A TA Instruments Discovery SDT 650 – Simultaneous DSC-TGA was used to collect the differential scanning calorimetry (DSC) data. Approximately 9 mg of sample was placed in a 90 µL alumina pan, and the sample was heated to 600 ºC at 10 ºC/min under nitrogen.

RESULTS AND DISCUSSION

$NbTe_4$ particles were synthesized by heating a mixture of diphenyl ditelluride and $NbCl_5$ in oleylamine at 340 °C for 1 hour under an Ar atmosphere, as described in detail in the Experimental Section. Figure 1a shows the powder XRD pattern for the product isolated from this reaction, along with a reference pattern for $NbTe_4$. All experimentally observed peaks match those of the reference pattern, as confirmed by the indexing that is included in Figure 1a. The relative intensities match well, except for a slight enhancement of the (*h*00) peaks that is attributed to a minor preferred orientation. Additionally, the sharp peaks in the XRD pattern indicate that the $NbTe_4$ product is highly crystalline and consists of large crystallites. Consistent with this observation, the SEM image of the $NbTe_4$ product in Figure 1b shows submicron and micron scale particles with an overall rectangular shape and cross section. The large particle sizes observed by SEM correlate to the sharp XRD peaks, and the preferred orientation observed by XRD correlates to the anisotropic morphology seen in the SEM image. The corresponding SEM-EDS element maps in Figure 1b confirm co-localization of Nb and Te over the large scale of the image, with no evidence of amorphous components or secondary phases that contain only Nb or Te, as would have been the case if significant amounts of amorphous niobium oxide or tellurium oxide were present. Analysis of the accompanying EDS spectrum (Figure 1c) confirms a ~1:4 ratio of Nb:Te, which is consistent with the expected composition of $NbTe_4$. Taken together, the data in Figure 1 confirm the formation of $NbTe_4$ as submicron to micron-scale particles. By substituting $TaCl_5$ for $NbCl_5$, we were also able to generate a sample containing a small amount of $TaTe_4$ (Figure S1), which has the same crystal structure as $NbTe_4$. While demonstrating the potential accessibility of $TaTe_4$ using a solvothermal reaction, we focused on $NbTe_4$, which is discussed exclusively below.

To access the highest-purity samples of $NbTe_4$, based on XRD and composition analysis, we needed to use a 1.5- to 2-fold excess of $NbCl_5$; otherwise, a byproduct of crystalline elemental tellurium was always observed by XRD (Figure S2). This observation suggested that perhaps tellurium may be forming first during the reaction *en route* to forming $NbTe_4$. Indeed, upon injection of the $NbCl_5$, diphenyl ditelluride, and oleylamine precursor mixture into the reaction flask at 340 °C, the diphenyl ditelluride decomposed to form elemental Te needles that fell out of solution due to their large size. As the reaction progressed, the particles resuspended, correlating with the formation of $NbTe_4$. To confirm that the elemental Te needles that fell out of solution were not influenced by the $NbCl_5$ precursor, we performed a control reaction with just the diphenyl ditelluride, and the product was similar Te needles, as confirmed by XRD and SEM (Figure S3).

To gain additional insights into how the $NbTe_4$ particles are formed, we probed the evolution of the reaction by characterizing samples isolated at time points of 15, 30, 45, and 60 minutes.

Figure 2a shows powder XRD patterns, along with SEM images and SEM-EDS element maps in Figure 2b, for the samples isolated at each time point; additional SEM images are included in Figure S4 of the Supporting Information. For the sample isolated at 60 minutes, the powder XRD pattern matches crystalline $NbTe_4$ without any detectable impurities. Likewise, the SEM and SEM-EDS data show that Nb and Te are evenly distributed and colocalized across the sample, similar to that shown in Figure 1. However, for the sample isolated at 15 minutes, the powder XRD pattern matches with elemental tellurium, without any evidence of $NbTe_4$ formation. Additionally, the accompanying SEM image shows large and faceted needles with widths ranging from approx. 1 to 5 μm and lengths in excess of 35 μm, along with some smaller fragments. Some of these needles are oriented such that we can view their cross sections; many are hollow, exhibiting a hexagonal cross section, as shown by the blue inset in Figure 2b. (The control experiment using only diphenyl ditelluride, without $NbCl_5$, also produces needles with a hollow cross section, indicating that this morphological feature is intrinsic to Te formation rather than due to Nb incorporation.) In addition to the needles, numerous spherical and near-spherical particles are observed. Spherical tellurium particles are commonly observed as intermediates in syntheses that yield one-dimensional tellurium nanostructures. In the literature, these particles are implicated as seeds from which the one-dimensional tellurium needles grow.[21] As a result, the spherical tellurium particles are often attached to the tellurium needles that grow from them; such behavior is indeed observed in Figure 2b. The corresponding SEM-EDS element map shows that tellurium is associated with both the needles and the spherical particles, while niobium is present only at background levels throughout.

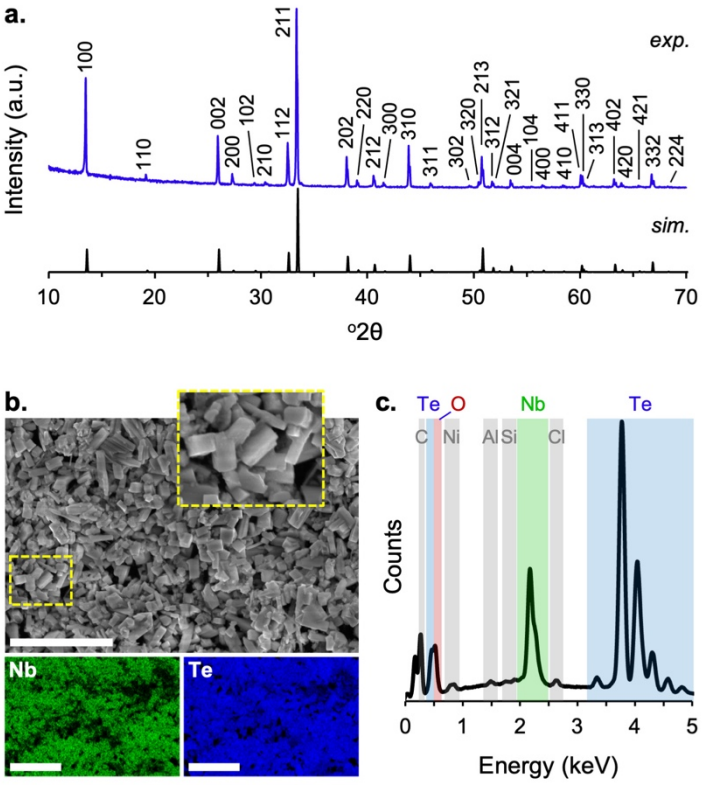

Figure 1. (a) Experimental and indexed powder XRD pattern for as-synthesized $NbTe_4$ (blue, top) and the corresponding reference pattern (black, bottom) from ICSD-43282 (ICSD release 2024.1).[15] (b)

Representative SEM image of the $NbTe_4$ particles and corresponding EDS element maps for Nb Lα and Te Lα. Scale bars are 10 μm. (c) EDS spectrum corresponding to the SEM image in (b). The Nb, Te, and O signal regions are highlighted in green, blue, and red, respectively. Adventitious signals corresponding to C, Ni, Al, Si, and Cl are shown as well. These signals arise from the carbon tape and SEM stub, as well as residual Cl from the $NbCl_5$ reagent.

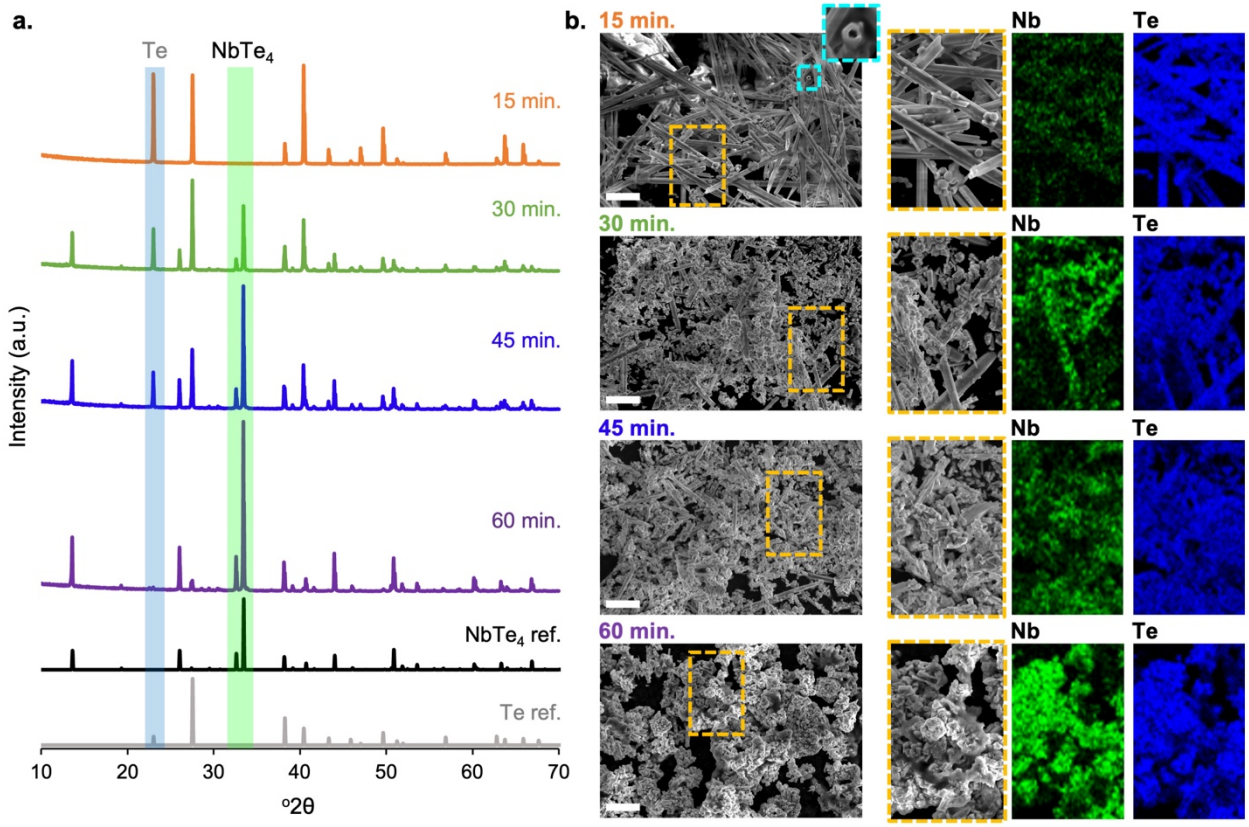

Figure 2. (a) XRD patterns for samples isolated at time points of 15, 30, 45, and 60 minutes during the synthesis of $NbTe_4$, showing a progression from Te to $NbTe_4$. The blue highlighted region corresponds to a diagnostic peak for tellurium [ICSD-65692 (ICSD release 2024.1)][20] and the green highlighted region corresponds to a set of diagnostic peaks for $NbTe_4$ [ICSD-43282 (ICSD release 2024.1)].[15] (b) Representative SEM images for the samples isolated at each time point, along with corresponding EDS element maps of Nb Lα and Te Lα for the regions indicated by the orange dashed box. The enlarged region outlined in blue in the 15 minute sample shows the hollow hexagonal cross section of a tellurium needle. Scale bars are 15 μm.

We now turn to the samples isolated at time points of 30 and 45 minutes. For the 30-minute sample, the most intense peak in the XRD pattern corresponds to tellurium, with the other peaks matching $NbTe_4$. The accompanying SEM image and SEM-EDS element map show evidence of Te needles analogous to those observed at 15 minutes, which appear to contain tellurium but not niobium. Additionally, the SEM and SEM-EDS data reveal smaller particles that are reminiscent of the spherical tellurium particles in the 15-minute sample based on their size, but they now appear as multi-faceted variants. These particles contain both tellurium and niobium and are morphologically related to some of the $NbTe_4$ particles that were observed after 60 minutes. By 45 minutes, the XRD data shows that tellurium is still present, but the majority phase is now $NbTe_4$.

SEM and SEM-EDS indicate that some tellurium needles remain present but most of the sample is consistent with the smaller $NbTe_4$ particles that contain co-localized tellurium and niobium. Several needles that are reminiscent of those seen in the 15-minute sample now appear degraded into smaller pieces, including some that are split open so that the hollow interior is now visible.

This gradual progression from only tellurium at 15 minutes to increasing amounts of $NbTe_4$ (with tellurium still present) at 30 and 45 minutes and then to exclusively $NbTe_4$ at 60 minutes is captured in the EDS spectra that are shown in Figure 3a. A morphological progression is also evident; representative regions of the SEM images from Figures 2b and S4 are shown in Figure 3b. These images show several key features. First, throughout the course of the reaction, faceted growths begin to appear on both the tellurium needles and on the spherical tellurium particles. We assume that the faceted structures are $NbTe_4$, as the onset of these particles by SEM correlates with the onset of $NbTe_4$ by XRD and the emergence of Nb by EDS. On the needles, some structures appear very thin, with very little contrast against the needles onto which they are growing, while others appear to be thicker. Most of the faceted particles on the needles are rectangular and oriented either parallel to the long axis of the needles or at angles of approx. 127°, 111°, and 146° relative to the diameter of the needles. These angles correspond to the $(30\bar{3})$, $(20\bar{1})$, and $(10\bar{2})$ planes of Te, respectively. On the spherical tellurium particles, the faceted growths seem to almost cover the original particles completely, but again, the structures are predominantly rectangular.

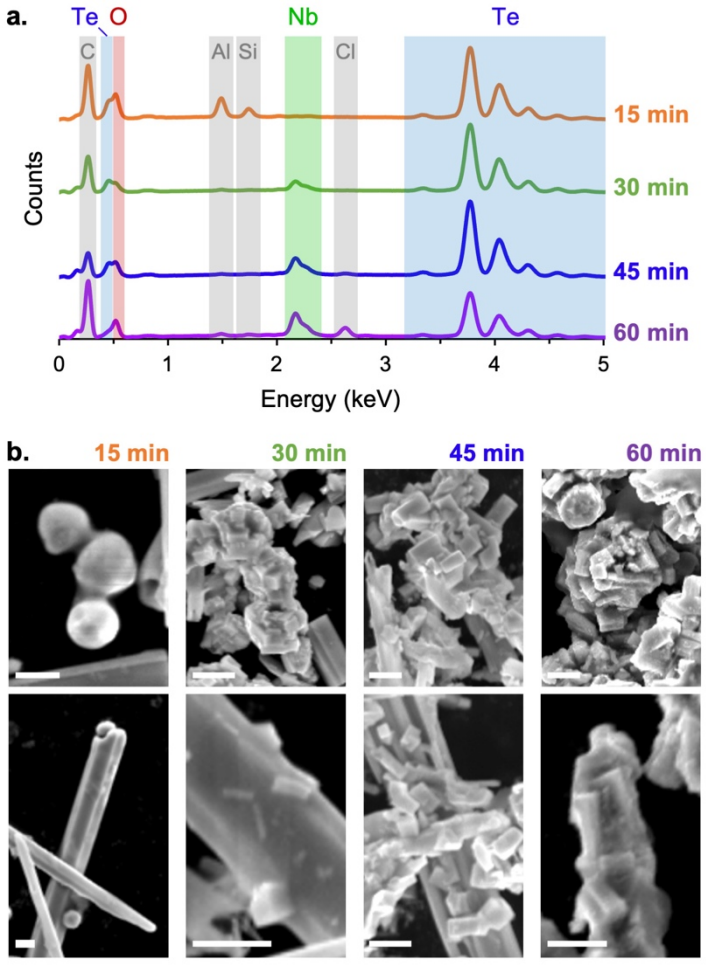

Figure 3. (a) EDS spectra corresponding to the time point samples in Figure 2b. The highlighted Nb peak increases in intensity over time, which correlates with increasing amounts of Nb diffusing into the material. (b) SEM images of selected regions for each time point, showing features consistent with the transformation of pseudo-spherical Te particles and Te needles at 15 minutes to $NbTe_4$ particles at 60 minutes. Complete SEM images are included in Figure S4 of the Supporting Information. Scale bars are 2 μm.

To better understand how the Te needles transform to $NbTe_4$ particles, and to begin to rationalize both their morphologies and their orientations relative to the Te needles on which they grow, we used HAADF-STEM imaging along with STEM-EDS element mapping to analyze the spatial composition distribution in samples isolated at 30-, 45-, and 60-minute time points. Figure 4a shows a HAADF-STEM image of part of a needle onto which the growth of a different nanoscale material appears to be occurring. The accompanying STEM-EDS maps for Te and Nb confirm that the needle contains only tellurium and that the growth has both tellurium and niobium. Notably, the niobium signal is most intense around the edges of the growth, as is evident both in the STEM-EDS element map for Nb and in the line scan. The oxygen signal is flat and at background levels. The particle isolated at the 45-minute time point, shown in Figure 4b, is rectangular and is not connected to a larger needle. The STEM-EDS map for Te shows consistent and uniform signal throughout the particle. This interpretation is validated by the corresponding line scan, which shows a nearly flat and high Te signal across the entire particle. In contrast, the STEM-EDS map for Nb shows the highest signal around the edges, similar to what we observed in Figure 4a. However, in Figure 4b, the Nb signal also penetrates partially into the particle at an angle. In this region the Nb:Te ratio is approximately 1:4, which is consistent with $NbTe_4$. There also appears to be a very thin shell of oxygen co-localized with niobium along the outer edge of the particle, suggesting the presence of a thin niobium oxide shell. Finally, in the sample isolated at 60 minutes, the particle shown in Figure 4c has a uniform distribution of both Nb and Te throughout with a Nb:Te ratio of approx. 1:4, corresponding to $NbTe_4$; the thin niobium oxide shell observed in the 45-minute sample persists in the 60-minute sample. The STEM-EDS spectra for the time point particles similar to Figure 3b are shown in Figure S5.

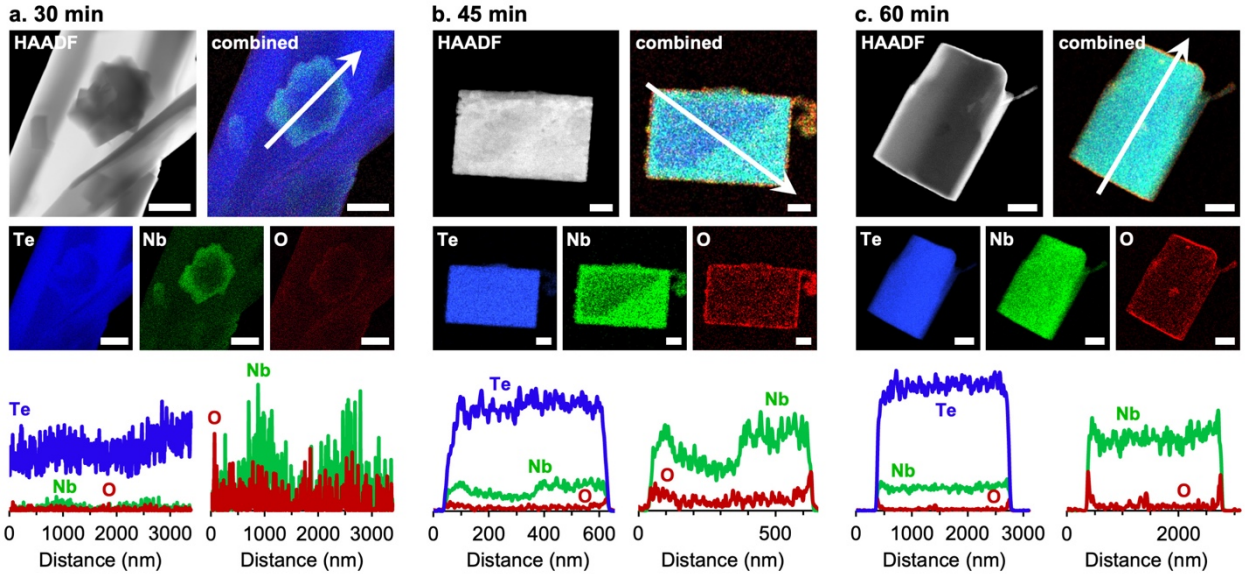

Figure 4. HAADF-STEM images and corresponding STEM-EDS element maps of Te Lα, Nb Lα, and O Kα for samples isolated at (a) 30 minutes (1 μm scale bars), (b) 45 minutes (100 nm scale bars), and (c) 60 minutes (500 nm scale bars). For each time point, line scans corresponding to the white arrows in the

combined maps are also shown. The line scans are shown below each set of images with and without Te to better observe the Nb and O signals.

Several aspects of the data shown in Figure 4 are notable. First, the Nb-Te growth on the Te needle in Figure 4a has well defined facets, several of which appear to align with various angles on the underlying Te needle. The orientations are similar to those observed by SEM in Figures 2 and 3. Second, the size of the Nb-Te growth in Figure 4a is much smaller than the size of the Te needles; the sizes of the Te/$NbTe_4$ and $NbTe_4$ particles in Figure 4b and 4c are smaller than the Te needles as well. The morphologies of the Nb-Te, Te/$NbTe_4$, and $NbTe_4$ particles in Figure 4 are also reminiscent of those in Figures 1 and 2. Therefore, based on both size and morphology, all three Nb-Te particles in Figure 4 are more in line with the $NbTe_4$ particles observed in the data shown in Figures 1 and 2 than with the size and morphology of the Te needles.

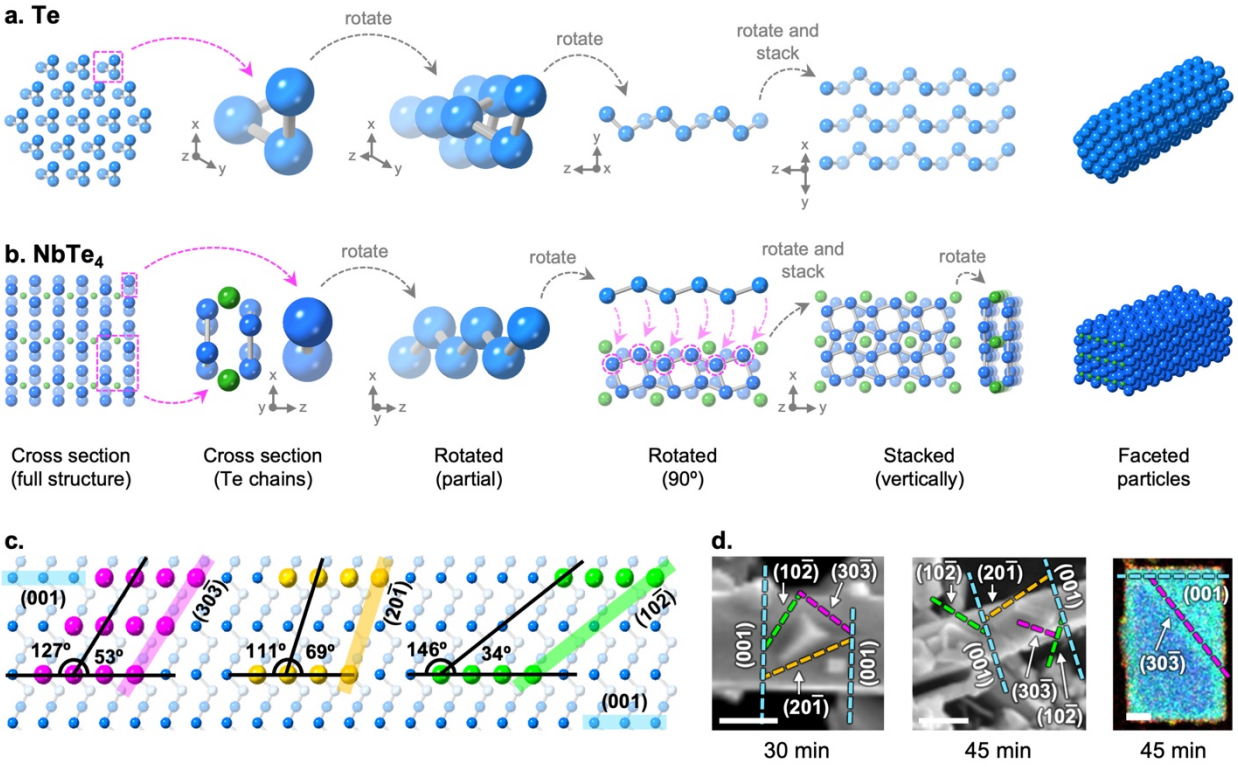

Figure 5. Cross sectional views of the crystal structures of (a) Te and (b) $NbTe_4$ in structurally comparable directions. The similarities and differences between the Te chains in Te and in $NbTe_4$ are highlighted by extracting them from the structures and rotating them in various directions. By comparing the Te vs $NbTe_4$ structural features, the transformation from Te needles with a hexagonal cross section to $NbTe_4$ particles with a rectangular cross section becomes evident. (c) A cross-sectional view of the (010) plane of Te. Te atoms are shown in blue, with the dark blue atoms in the same plane (*i.e.*, forming the top layer). Superimposed onto the Te (010) plane are the $(30\bar{3})$ plane in pink, the $(20\bar{1})$ plane in yellow, the $(10\bar{2})$ plane in green, and the (001) plane in blue. Relevant angles between these planes and the adjacent Te atoms in the (010) plane are also shown. (d) SEM images of selected regions from the 30 and 45 minute samples, along with the 45-minute STEM-EDS element map that was previously shown in Figure 4b. Superimposed on these images are solid lines corresponding to the edges of $NbTe_4$ deposits on Te, labeled and color coded based on the Te planes they correspond to (given the observed angles). The scale bars from left to right are 1 μm, 2 μm, and 100 nm.

Given the observations in Figures 2, 3, and 4, we turn to crystal structure relationships to help rationalize the pathway by which the $NbTe_4$ particles form as well as the evolution of morphology based on both the SEM and STEM-EDS data. Figures 5a and 5b show models of a small subunit of the Te needles and $NbTe_4$ rectangular particles, respectively. Both are oriented in a way that is consistent with the preferred orientation observed by XRD in Figures 1 and 2, as well as literature knowledge of the growth mechanism of tellurium needles. The structures of both the cross sections and the exposed facets for Te and $NbTe_4$ are also shown in Figure 5a and 5b, along with enlargements of the Te chains that comprise each structure, rotated in different orientations to show the view from both the cross section and the exposed facets. Both Te and $NbTe_4$ contain one-dimensional bonded chains of tellurium atoms. In Te, these tellurium chains appear as a hexagonal array of triangles when viewed along the cross section. However, closer inspection shows that the Te atoms twist in a spiral along the length of the Te needles. The structure of $NbTe_4$ is related, as it also has chains of bonded tellurium atoms, but here they are rearranged into a zigzag structure with alternating short and long bonds. The tellurium chains in $NbTe_4$ are also arranged in a rectangular motif rather than the hexagonal array in Te.

Combining the structural relationships between Te and $NbTe_4$ with the diffraction and microscopy data in Figures 1, 2, 3, and 4, we can rationalize a bit more about how the reaction occurs. The data confirms that Te forms first in the reaction and that Nb incorporates over time. The SEM images in Figure 3 show $NbTe_4$ growing in a small number of orientations on Te substrates, suggesting a crystallographic relationship between the growing $NbTe_4$ and the Te on which it is growing. These growth directions match with the orientations predicted based on the crystallographic planes exposed on the Te needle facets, as shown in Figure 5c. The SEM images from the 30- and 45-minute samples and the STEM-EDS map of the 45-minute sample from Figure 4b, which is an intermediate structure that appears to show an angled interface between $NbTe_4$ and Te, are again shown in Figure 5d along with their crystallographic planes superimposed. Their growth angles are color coded to match the plane they best match. Analysis of the SEM images for the samples isolated at 30 and 45 minutes reveals that the $NbTe_4$ particles adopt growth angles of approx. 127° and 131°, which match well with the angles associated with the $(30\bar{3})$ plane. Additionally, the 30-minute sample has an angle of 146°, matching the angle of the $(10\bar{2})$ plane, and the 45-minute sample contains an angle of 110°, corresponding to the $(20\bar{1})$ plane. In the STEM-EDS map, the angle at which Nb diffusion appears to propagate is 129°, which is consistent with that expected for the $(30\bar{3})$ plane. This observation suggests that niobium is preferentially diffusing into the tellurium such that it propagates in these directions.

Diffusion channels perpendicular to these angled planes correlate with preferred locations where the niobium atoms could insert to form $NbTe_4$. We therefore propose that Te forms first and then converts, through niobium diffusion along preferred crystallographic directions, into $NbTe_4$. The diffusion is observed to initiate only on the sides of the needles rather than the end. We attribute this to the crystallographic relationships between $NbTe_4$ and Te, as well as the fact that the solution-mediated diffusion would occur on a more reasonable length scale of a few hundred nanometers to a micron on the cross section instead of tens of microns through the length of the needles. Two diffusion pathways appear to occur simultaneously during the reaction. The first occurs when $NbTe_4$ growth initiates on the surface of the Te needles. The STEM-EDS map for the 30-minute STEM-EDS map in Figure 4a indicates the initial stages of $NbTe_4$ growth, in which there are smaller particles containing Nb on the surface of the larger needles. The contrast differences in the HAADF image and the Te map are due to the Te needle being hollow and the subsequent growth on the surface of the needle, respectively. As the reaction progresses, the $NbTe_4$ particles

attached to the Te needles appear to grow before breaking off to form individual particles. For this process to occur, Te must diffuse from the interior to the surface of the Te needle for it to propagate outward, which is a common interfacial diffusion process. The localization of Nb on the surface of the particles shown in Figures 4a and 4b hints at such a process involving the simultaneous diffusion of Te out of the needle and Nb into the particle.

When this process occurs, the positioning of the Nb can help facilitate the spiral Te chains in Te to shift slightly to form the zigzag chains in $NbTe_4$, with a concomitant shift from the hexagonal array of chains in Te to the rectangular array in $NbTe_4$. Such a structural transformation would only require minor localized rearrangements to occur, and therefore would be favorable under the reaction conditions, which have sufficient thermal energy for diffusion to occur but insufficient thermal energy for a large-scale structural change to happen. A larger-scale structural change would be required to instead form other niobium tellurides, such as $NbTe_2$, Nb_3Te_4, Nb_5Te_4, or Nb_3Te, but these products are not observed. This process also rationalizes the shift from Te needles with a hexagonal cross section to $NbTe_4$ particles with a rectangular cross section, in addition to the reason that the $NbTe_4$ particles are much smaller than the Te needles from which many of them are derived. While the structural rearrangements are minor and localized, over large distances they will create significant strain, due both to lattice mismatch and an evolving morphological preference. This strain will then cause fracturing, which will break apart the larger Te particles into smaller $NbTe_4$ particles, as is observed in the SEM images. We note that in the literature, metal telluride syntheses that occur *via* metal diffusion through preformed Te nanowires often retain the original morphology.[22] However, those nanowires are much smaller in diameter than ours and the reactions do not appear to be diffusion limited. Here, the micron scale Te needles offer a template that is too large for diffusion to fully occur in solution without the strain that arises from differences in the crystal structures leading to its fracturing into smaller particles.

In addition to the time point study, the effects of temperature, solvent, and injection method were also probed. At 340 °C, the diphenyl ditelluride decomposes rapidly to form elemental Te needles, as mentioned earlier (Figure S3). Decreasing the reaction temperature to 300 °C and 275 °C while keeping all other reaction conditions constant, we found that a mixture of Te and $NbTe_4$ formed. At both temperatures, Te was the major product and was always present; pure $NbTe_4$ was not achievable at these lower temperatures with the reaction time of 1 hour remaining constant, as shown in Figure S6. It is possible that a phase pure $NbTe_4$ product could be made to form over a longer time, if desired. This observation is consistent with a diffusion-based process, as Te forms readily at all temperatures studied but the amount of incorporated Nb increases with increasing temperature. Next, instead of using oleylamine as the solvent, we used 1-octadecene at 300 °C and oleic acid at 340 °C; the reaction temperature in 1-octadecene was decreased to accommodate its lower boiling point. Both experiments in these different solvents produced only elemental Te, based on the XRD data shown in Figure S7. Oleylamine as a solvent is more reducing than either 1-octadecene or oleic acid, suggesting that the stronger reducing environment provided by the oleylamine is critical to the formation of $NbTe_4$. Finally, we probed the proposed diffusion pathway by temporally separating the formation of elemental Te with the introduction of the niobium reagent. Instead of injecting the $NbCl_5$ and the diphenyl ditelluride simultaneously, the $NbCl_5$ was injected into the heated oleylamine and held for 30 minutes, and then the diphenyl ditelluride was injected and held at 340 °C for an additional 15, 30, and 45 minutes. The initial reaction time of 30 minutes was chosen based on that being the time point in which Nb diffusion was first observed. As mentioned previously, the diphenyl ditelluride decomposes upon injection into the hot oleylamine and the $NbTe_4$ particles begin suspending

around 30 minutes after the injection is complete. This observation led us to choose holding the $NbCl_5$ for 30 minutes to allow the Nb to form its reactive species that promotes diffusion. The XRD patterns in Figure S8 show that the amount of elemental Te decreases from 15 to 30 minutes, forming $NbTe_4$ at 45 minutes. This behavior is consistent with the proposed diffusion pathway because there is evidence (by XRD) that Te needles are present along with $NbTe_4$ at the 15- and 30-minute time points.

Given these insights into the pathway by which the $NbTe_4$ particles form, we next sought to better understand the surface composition, given that diffusion processes begin at the surface and also a thin niobium oxide shell was observed by STEM-EDS mapping in Figure 4. To probe the nature of the oxide that was present at the surface of the particles just after synthesis and progressively over time, we compared the XRD patterns and XPS spectra of a freshly synthesized sample to a sample that had been stored for one month (Figure 6). The Nb 3d and Te $3d_{5/2}$ regions for the fresh sample are shown in Figure 6a. While the Nb 3d region was fit with three sets of peaks corresponding to both Nb $3d_{5/2}$ and Nb $3d_{3/2}$, for this discussion, we will only consider Nb $3d_{5/2}$ for simplicity. The peaks corresponding to $NbTe_x$, NbO_x, and Nb_2O_5 have peak positions at 203.2, 205.1, and 207.4 eV, respectively. The amount of the sample that was oxidized was determined by quantifying the Nb $3d_{5/2}$ peaks for Nb_2O_5 and NbO_x, which are 9.8% and 5.1%, respectively. As the experimental peak position falls between that of NbO (203.9 eV) and NbO_2 (205.9 eV), we can assume that there is a mixture of the two oxides, which we denote as NbO_x. Theoretically, there would need to be 32.1% oxygen to account for all of the Nb oxides; the experimentally determined percentage of 30.1% matches well with the theoretical value. (Quantification data are shown in Table S1.)

In the Te $3d_{5/2}$ region, there is a single peak at 572.6 eV. Literature reports for the XPS peak positions for a variety of niobium chalcogenides, niobium metal, and tellurium metal indicate Nb $3d_{5/2}$ peak positions for Nb_3Te_4, $NbTe_4$, and Nb^0 of 203.0, 204.0, and 202.0 eV, respectively and the Te $3d_{5/2}$ peak positions for Nb_3Te_4, $NbTe_4$, and Te^0 at 572.8, 573.0, and 573.4 eV, respectively.[23] Considering neither the peak in the Nb $3d_{5/2}$ region nor in the Te $3d_{5/2}$ region perfectly matches the reference values for Nb_3Te_4 or $NbTe_4$, we account for the slight variations in the reference and experimental peak positions by focusing on the difference in peak positions. The differences in reported peak positions (Te $3d_{5/2}$ – Nb $3d_{5/2}$) for Nb_3Te_4, $NbTe_4$, and Te versus Nb metal are 369.8, 369.0, and 371.4 eV, respectively, while the difference for our fresh sample of $NbTe_4$ is 369.4 eV. We can rule out the signal coming from elemental Nb and Te as our experimental difference value is 2.0 eV lower than the reported value of 371.4 eV. Conversely, the difference in peak positions fall between those of $NbTe_4$ and Nb_3Te_4 which suggests that both could be present on the surface of the particles. This is a reasonable assumption as the XPS quantification yields a Te:Nb ratio of 2.6, which is greater than the Te:Nb ratio in Nb_3Te_4 ratio but less than the Te:Nb ratio in $NbTe_4$, indicating that both species could be present. Considering that excess Nb was added into the reaction and the formation of an amorphous niobium oxide species was subsequently observed, it is rational to conclude that there exists an amorphous niobium rich telluride, with a composition of approximately Nb_3Te_4, in addition to the crystalline $NbTe_4$.

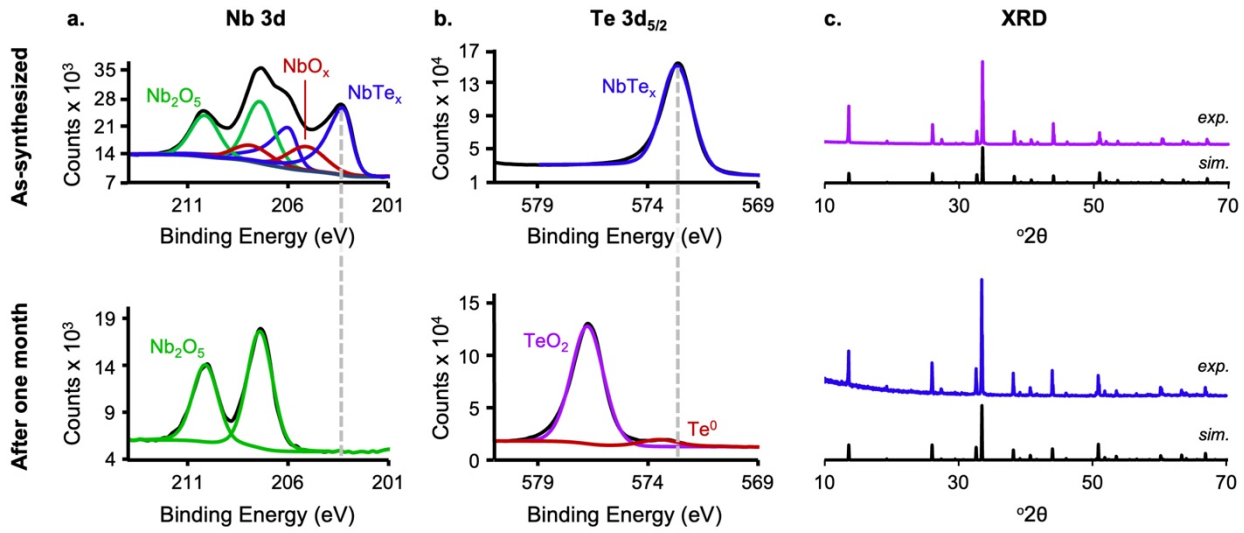

Figure 6. XPS spectra of the (a) Nb 3d and (b) Te $3d_{5/2}$ regions, as well as (c) experimental XRD patterns with simulated $NbTe_4$ reference patterns [ICSD-43282 (ICSD release 2024.1)],[15] for a freshly prepared $NbTe_4$ sample (top) and a sample that was stored for one month (bottom). The dotted lines in each region of the XPS spectra correspond to the primary $NbTe_x$ peaks.

After storage in ethanol for one month, the surface chemistry of the $NbTe_4$ particles changed, as shown by the XPS data in Figure 6a and 6b. The Nb 3d region is fit with one set of peaks corresponding to Nb_2O_5, with a Nb $3d_{5/2}$ peak position of 207.4 eV. The Te $3d_{5/2}$ region is fit with two peaks corresponding to TeO_2 at 576.7 eV and a small amount of Te^0 at 573.5 eV. The XPS data therefore indicates a change in surface oxide chemistry from primarily niobium oxides and $NbTe_x$ as synthesized to amorphous TeO_2 and Nb_2O_5 after one month. To rationalize the surface chemistry evolution, we first note that the surface of the $NbTe_4$ particles contains an amorphous Nb-rich oxide shell, as seen in the STEM-EDS maps in Figure 4 and as discussed above. This amorphous oxide shell then undergoes a transformation to being primarily TeO_2, while still having an appreciable amount of Nb_2O_5. This change is attributed to the tendency for surface tellurium atoms to oxidize over time in metal tellurides.[24] Additionally, it has been observed that tellurium atoms just below the surface within a particle will leach out of the structure and migrate to the surface to oxidize, which is also consistent with our observations here.[18] Finally, the stability of the bulk sample was probed by XRD to complement the XPS analysis. The XRD pattern for the bulk sample in Figure 6c indicates that crystalline $NbTe_4$ remains present even after one month of storage, despite the surface oxidation observed by XPS. As the particles are hundreds of nanometers to ~1 micron in all dimensions, the XPS penetration depth of a few nanometers only provides information for the surface of the material, which highlights the tendency for the surface to change in composition over time while the bulk of the particles remains the same. This result suggests that the oxide is passivating, preventing degradation of the crystalline $NbTe_4$.

Finally, given the potential interest in $NbTe_4$ as a phase change material, we used differential scanning calorimetry (DSC) to characterize the thermal behavior of our $NbTe_4$ sample and to compare it to sputtered $NbTe_4$ films reported in the literature. A DSC heating curve of a sample of $NbTe_4$ particles, shown in Figure S9, reveals an endothermic transition at 447 °C, which is analogous to that reported previously for a sputtered film of amorphous $NbTe_4$ that was annealed at 272 °C to form crystalline $NbTe_4$. The Nb-Te phase diagram shows that $NbTe_4$ decomposes

around 450 °C, and an experimental study indicates a decomposition temperature of 443 °C. Elemental tellurium, which has a melting point of 449.5 °C, is a decomposition product of $NbTe_4$.[25] Consequently, the thermal behavior of $NbTe_4$ in the range of 440–450 °C is quite complex and challenging to deconvolute, but what we observe is consistent with what is expected based on existing literature.

CONCLUSIONS

In summary, we reported the solvothermal synthesis of $NbTe_4$ using readily available reagents and mainstream colloidal nanocrystal synthesis techniques. As such, this demonstration represents a rare example of a solvothermal route to a group V transition metal telluride. The $NbTe_4$ particles form through a multi-step pathway that occurs *in situ*, beginning with the initial formation of tellurium needles and then the subsequent initiation of $NbTe_4$ growth through a diffusion-based pathway. The deposition of $NbTe_4$, which occurs concomitantly with the consumption of the tellurium needles, occurs along characteristic angles that relate to the crystal structures of both Te and $NbTe_4$. As a result of the crystallographic relationships between the tellurium needles and the $NbTe_4$ product, we were able to rationalize how the $NbTe_4$ particles formed and how their morphology developed and evolved. These insights are important, as they define and rationalize a solvothermal pathway to tellurium-rich group V metal tellurides, which are of interest as nano- and micro-scale particles for both their exotic low-temperature electronic properties and their potential applications as thermoelectrics, catalysts, and phase change materials. In addition, understanding the crystallographic relationships between Te and $NbTe_4$, and their role in rationalizing both the reaction pathway and the particle morphology, helps to inform how the synthesis of certain phases can be targeted by taking their crystal structures into account. We also find that the surface of the $NbTe_4$ particles oxidizes over time, but the $NbTe_4$ remains unchanged. This observation bodes well for overall stability of the $NbTe_4$ particles for applications.

ASSOCIATED CONTENT

SUPPORTING INFORMATION

The Supporting Information is available free of charge at http://pubs.acs.org.

Additional SEM, STEM-EDS, XRD, DSC, and crystallographic data (PDF)

AUTHOR INFORMATION

Corresponding Authors

Raymond E. Schaak – *Department of Chemistry*, *Department of Chemical Engineering*, and *Materials Research Institute*, *The Pennsylvania State University, University Park, Pennsylvania 16802, United States*; Email: res20@psu.edu

Mauricio Terrones –*Department of Chemistry*, *Department of Physics, Department of Materials Science and Engineering, and Center for 2-Dimensional and Layered Materials*, *The Pennsylvania State University, University Park, PA 16802, United States;* Email: mut11@psu.edu

Authors

Katherine L. Thompson – *Department of Chemistry*, *The Pennsylvania State University, University Park, Pennsylvania 16802, United States*

Peyton L. Herring – *Department of Chemistry*, *The Pennsylvania State University, University Park, Pennsylvania 16802, United States*

Notes

The authors declare no competing financial interest.

ACKNOWLEDGEMENT

This work was supported by the U.S. National Science Foundation under grant DMR-2210442. XRD, SEM, STEM, XPS, and DSC data were acquired at the Materials Characterization Lab of the Penn State Materials Research Institute. The authors thank Zhuohang Yu for assisting with the XPS data collection, Jeff Shallenberger for assisting with the XPS analysis, Dean Anderson for collecting the DSC data, and Gaurav Dey for helpful discussions.

REFERENCES

(1) Chen, B.; Kruse, M.; Xu, B.; Tutika, R.; Zheng, W.; Bartlett, M. D.; Wu, Y.; Claussen, J. C. Flexible Thermoelectric Generators with Inkjet-Printed Bismuth Telluride Nanowires and Liquid Metal Contacts. *Nanoscale* **2019**, *11* (12), 5222–5230.

(2) Nan, B.; Song, X.; Chang, C.; Xiao, K.; Zhang, Y.; Yang, L.; Horta, S.; Li, J.; Lim, K. H.; Ibáñez, M.; Cabot, A. Bottom-Up Synthesis of SnTe-Based Thermoelectric Composites. *ACS Appl. Mater. Interfaces* **2023**, *15* (19), 23380–23389.

(3) Xu, J.; Li, H.; Du, B.; Tang, X.; Zhang, Q.; Uher, C. High Thermoelectric Figure of Merit and Nanostructuring in Bulk $AgSbTe_2$. *J. Mater. Chem.* **2010**, *20* (29), 6138–6143.

(4) Cheng, M. K.; Ng, C. Y.; Ho, S. L.; Atanov, O.; Tai, W. T.; Liang, J.; Lortz, R.; Sou, I. K. Interfacial Superconductivity and Zero Bias Peak in Quasi-One-Dimensional $Bi_2Te_3/Fe_{1+y}Te$ Heterostructure Nanostructures. *Adv. Elect. Materials* **2023**, *9* (4), 2200943.

(5) Li, H.; Li, C.; Tao, B.; Gu, S.; Xie, Y.; Wu, H.; Zhang, G.; Wang, G.; Zhang, W.; Chang, H. Two-Dimensional Metal Telluride Atomic Crystals: Preparation, Physical Properties, and Applications. *Adv. Funct. Materials* **2021**, *31* (23), 2010901.

(6) Nath, M.; De Silva, U.; Singh, H.; Perkins, M.; Liyanage, W. P. R.; Umapathi, S.; Chakravarty, S.; Masud, J. Cobalt Telluride: A Highly Efficient Trifunctional Electrocatalyst for Water Splitting and Oxygen Reduction. *ACS Appl. Energy Mater.* **2021**, *4* (8), 8158–8174.

(7) Sadaqat, M.; Nisar, L.; Babar, N.-U.-A.; Hussain, F.; Ashiq, M. N.; Shah, A.; Ehsan, M. F.; Najam-Ul-Haq, M.; Joya, K. S. Zinc-Telluride Nanospheres as an Efficient Water Oxidation Electrocatalyst Displaying a Low Overpotential for Oxygen Evolution. *J. Mater. Chem. A*. **2019**, *7* (46), 26410–26420.

(8) Nukala, P.; Lin, C.-C.; Composto, R.; Agarwal, R. Ultralow-Power Switching via Defect Engineering in Germanium Telluride Phase-Change Memory Devices. *Nat. Commun*. **2016**, *7* (1), 10482.

(9) Zhang, F.; Zhang, H.; Krylyuk, S.; Milligan, C. A.; Zhu, Y.; Zemlyanov, D. Y.; Bendersky, L. A.; Burton, B. P.; Davydov, A. V.; Appenzeller, J. Electric-Field Induced Structural Transition in Vertical $MoTe_2$- and $Mo_{1-x}W_xTe_2$-Based Resistive Memories. *Nature Mater.* **2019**, *18* (1), 55–61.

(10) Nataj, Z. E.; Kargar, F.; Krylyuk, S.; Debnath, T.; Taheri, M.; Ghosh, S.; Zhang, H.; Davydov, A. V.; Lake, R. K.; Balandin, A. A. Raman Spectroscopy of Phonon States in $NbTe_4$ and $TaTe_4$ Quasi-one-dimensional van Der Waals Crystals. *J. Raman Spec.* **2024**, *55* (6), 695–705.

(11) De Lima, B. S.; Chaia, N.; Grant, T. W.; De Faria, L. R.; Canova, J. C.; De Oliveira, F. S.; Abud, F.; Machado, A. J. S. Large Enhancement of the CDW Resistivity Anomaly and Traces of Superconductivity in Imperfect Samples of $NbTe_4$. *Mater. Chem. Phys.* **2019**, *226*, 95–99.

(12) Yang, X.; Zhou, Y.; Wang, M.; Bai, H.; Chen, X.; An, C.; Zhou, Y.; Chen, Q.; Li, Y.; Wang, Z.; Chen, J.; Cao, C.; Li, Y.; Zhou, Y.; Yang, Z.; Xu, Z.-A. Pressure Induced Superconductivity

Bordering a Charge-Density-Wave State in $NbTe_4$ with Strong Spin-Orbit Coupling. *Sci Rep* **2018**, *8* (1), 6298.

(13) Wu, X.; Tao, Y.; Gao, Q.; Zhang, Y. Controllable Growth of $NbTe_4$ Micro/Nanostructures on Nb Substrates and Their Field-Emission Performance. *J. Mater. Chem*. **2009**, *19* (23), 3883.

(14) Shuang, Y.; Chen, Q.; Kim, M.; Wang, Y.; Saito, Y.; Hatayama, S.; Fons, P.; Ando, D.; Kubo, M.; Sutou, Y. $NbTe_4$ Phase-Change Material: Breaking the Phase-Change Temperature Balance in 2D Van Der Waals Transition-Metal Binary Chalcogenide. *Adv. Mater.* **2023**, *35* (39), 2303646.

(15) Selte, K.; Kjekshus, A.; Petersen, C. S.; Halvarson, H.; Nilsson, L. On the Crystal Structure of $NbTe_4$. *Acta Chem. Scand*. **1964**, *18*, 690–696.

(16) Zilevu, D.; Creutz, S. E. Solution-Phase Synthesis of Group 3–5 Transition Metal Chalcogenide Inorganic Nanomaterials. *Chem. Commun*. **2023**, *59* (57), 8779–8798.

(17) Fenton, J. L.; Fagan, A. M.; Schaak, R. E. General Solution-Phase Synthesis of Nanoscale Transition Metal Tellurides Using Metal Nanoparticle Reagents. *Eur. J, Inorg. Chem.* **2019**, *2019* (30), 3490–3493.

(18) Thompson, K. L.; Katzbaer, R. R.; Terrones, M.; Schaak, R. E. Formation and Transformation of $Cu_{2-x}Se_{1-y}Te_y$ Nanoparticles Synthesized by Tellurium Anion Exchange of Copper Selenide. *Inorg. Chem.* **2023**, *62* (11), 4550–4557.

(19) Penk, D. N.; Endres, E. J.; Nuriye, A. Y.; Macdonald, J. E. Dependence of Transition-Metal Telluride Phases on Metal Precursor Reactivity and Mechanistic Implications. *Inorg. Chem*. **2023**, *62* (9), 3947–3956.

(20) Adenis, C.; Langer, V.; Lindqvist, O. Reinvestigation of the Structure of Tellurium. *Acta Crystallogr. C Cryst. Struct. Commun.* **1989**, *45* (6), 941–942.

(21) Xi, G.; Peng, Y.; Yu, W.; Qian, Y. Synthesis, Characterization, and Growth Mechanism of Tellurium Nanotubes. *Cryst. Growth Des.* **2005**, *5* (1), 325–328.

(22) Liang, H.; Liu, S.; Wu, Q.; Yu, S. An Efficient Templating Approach for Synthesis of Highly Uniform CdTe and PbTe Nanowires. *Inorg. Chem.* **2009**, *48*, 4927-4933.

(23) Bahl, M. K. ESCA Studies of Some Niobium Compounds. *J. Phys. Chem. Solids* **1975**, *36* (6), 485–491.

(24) Lee, C.-H.; Silva, E. C.; Calderin, L.; Nguyen, M. A. T.; Hollander, M. J.; Bersch, B.; Mallouk, T. E.; Robinson, J. A. Tungsten Ditelluride: A Layered Semimetal. *Sci Rep*. **2015**, *5* (1), 10013.

(25) De Lima, B. S.; Chaia, N.; Correa, L. E.; Oliveira, F. S.; de Faria, L. R.; de Oliveira, I.; Coelho, G. C.; Machado, A. J. S. Experimental Study of the Binary Nb-Te System. *J. Phase Equilib. Diffus.* **2019**, *40* (5), 697–705.

Table of Contents Graphic

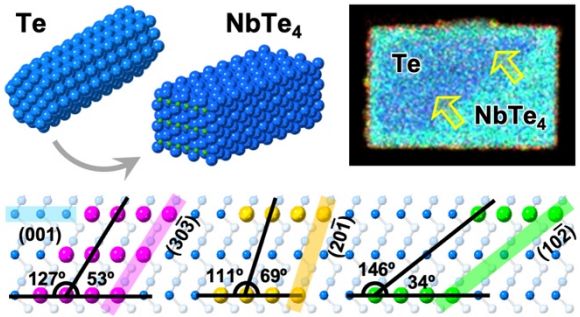

Synopsis: Colloidal particles of $NbTe_4$, a tellurium-rich metal telluride that exhibits a wide range of properties, were synthesized using a solvothermal route. $NbTe_4$ forms in solution through a multi-step pathway that involves the initial formation of elemental tellurium needles followed by niobium incorporation through a diffusion-based process. Crystal structure relationships between tellurium and $NbTe_4$ help to rationalize both the particle morphology and the synthetic pathway, including the direction in which diffusion occurs.